On-Line Monitoring of Mechanical Faults in Variable-Speed Induction Motor Drives Using the Wigner Distribution

Martin Blödt, *Student Member, IEEE*, David Bonacci, Jérémi Regnier, Marie Chabert, and Jean Faucher, *Member, IEEE*

***Abstract*—This paper deals with the detection of mechanical load faults in induction motors during speed transients. The detection strategy is based on stator current analysis. Mechanical load faults generally lead to load torque oscillations at specific frequencies related to the mechanical rotor speed. The torque oscillations produce a characteristic sinusoidal phase modulation of the stator current. Speed transients result in time-varying supply frequencies that prevent the use of classical, Fourier transform-based spectral estimation. This paper proposes the use of a time–frequency distribution, the Wigner Distribution, for stator current analysis. Fault indicators are extracted from the distribution for on-line condition monitoring. The proposed methods are implemented on a low-cost digital signal processor. Experimental results in a steady-state and during transients with load torque oscillations and load imbalance are presented.**

***Index Terms*—Digital signal processors (DSPs), fault detection, induction motor, load unbalance, mechanical fault, motor current signature analysis, torque oscillation, Wigner Distribution (WD).**

I. Introduction

INDUCTION motors are used in a wide variety of industrial applications. To increase the productivity, reliability and safety of an installation containing induction motors, permanent and automatic motor condition monitoring is often desired.

Stator current-based condition monitoring is advantageous due to its easy and economical implementation. The monitoring is usually done in a steady operation state using classical spectral analysis tools. However, many drives are adjustable speed drives where mechanical speed transients may be present during a long time period. The resulting time-varying supply frequency prevents the use of classical spectral analysis. Other signal processing methods such as time–frequency analysis allow condition monitoring during speed transients.

This paper investigates the detection of torque oscillations caused by mechanical faults in induction machines using stator current time–frequency analysis. In a general way, a fault in the load part of the drive gives rise to a periodic variation of the induction motor load torque. Examples for such faults causing torque oscillations include:

1) general fault in the load part of the drive system, e.g., load imbalance;
2) shaft misalignment;
3) gearbox faults, e.g., broken tooth;
4) bearing faults.

Torque oscillations already exist in a healthy motor due to space and time harmonics of the airgap field, but the considered fault-related torque oscillations are present at particular frequencies, often related to the shaft speed.

Thomson showed in [1] that mechanically-induced speed oscillations give rise to sidebands of the fundamental stator current frequency f_{s}. It was also demonstrated that shaft misalignment causes a rise at frequencies $f_{\mathrm{s}} \pm f_{\mathrm{r}}$ in the current spectrum where f_{r} is the shaft rotational frequency. Legowski *et al.* [2] studied the effects of an oscillating load torque on the stator current spectrum and instantaneous power. Kral *et al.* [3] analyzed the instantaneous motor input power to detect mass imbalance and eccentricity. Nevertheless, the power measurement requires three voltage levels and three current transducers. Obaid *et al.* [4] studied load imbalance and shaft misalignment and proposed a detection scheme based on monitoring stator current frequencies at $f_{\mathrm{s}} \pm f_{\mathrm{r}}$. All the cited works consider steady state motor operation at constant supply frequency. The proposed fast Fourier transform (FFT)-based spectral analysis cannot be performed during speed and frequency transients. Rotor faults in brushless DC motors are detected during transients using Wigner Distribution (WD) in [5]. However, the approach differs from the one proposed in this paper in the necessary current preprocessing and smoothing of the WD.

In this paper, the induction motor stator current is analyzed during transients, i.e., at variable supply frequencies using WDs based on previous work [6], [7]. It is shown that small load torque oscillations lead to a particular signature on the distribution. This signature is used to derive two different fault indicators. These methods are implemented on a low-cost

Manuscript received March 28, 2006; revised July 28, 2006.

M. Blödt was with the Laboratoire d'Electrotechnique et d'Electronique Industrielle (LEEI), Institut National Polytechnique de Toulouse, 31071 Toulouse, France. He is now with Siemens AG (e-mail: Martin.Blodt@leei.enseeiht.fr).

D. Bonacci is with the Télécommunications Spatiales et Aéronautiques (TéSA) Laboratory, 31071 Toulouse, France (e-mail: david.bonacci@tesa.prd.fr).

J. Regnier and J. Faucher are with the Electrical Engineering and Control Systems Department, Institut National Polytechnique of Toulouse, 31071 Toulouse, France, and also with the Laboratoire d'Electrotechnique et d'Electronique Industrielle, 31071 Toulouse, France (e-mail: jeremi.regnier@leei.enseeiht.fr; jean.faucher@leei.enseeiht.fr).

M. Chabert is with Ecole Nationale Supérieure d'Electrotechnique, d'Electronique, d'Informatique, d'Hydraulique et des Télécommunications, 31071 Toulouse, France (e-mail: Marie.Chabert@enseeiht.fr).

Digital Object Identifier 10.1109/TIE.2007.911941

0278-0046/$25.00 © 2008 IEEE

digital signal processor (DSP) to demonstrate their computational effectiveness.

Section II discusses the effect of load torque oscillations on the stator current. The resulting fault model shows a sinusoidal phase modulation (PM) at the fault characteristic frequency. In Section III, the chosen signal processing method, i.e., the WD is presented and the theoretical fault signature is calculated. Section IV deals with the DSP implementation of the proposed processing scheme, including the necessary filtering, downsampling, numerical calculation of the WD and the fault indicators. Section V describes the experimental set-up used to generate small periodic torque oscillations at the rotational frequency. The theoretically predicted fault signature on the WD is validated. Experimentally obtained fault indicators are presented for different fault levels under varying load conditions and in the steady and transient states. Furthermore, the WD-based indicators are compared to the classical spectrum-based approach in steady state to demonstrate their performance.

II. Stator Current Model Under Fault

The influence of the load torque oscillation on the stator current is studied using the magnetomotive force (MMF) and permeance wave approach. This approach is traditionally used for the calculation of the magnetic airgap field with respect to rotor and stator slotting or static and dynamic eccentricity [8], [9].

The detailed theoretical development for the stator current in case of load torque oscillations has been given in [10] to identify the consequence of bearing faults and in [6] for the general case. The results will be shortly resumed in the following.

As this paper considers variable speed drives, the supply frequency f_s and the fault frequency f_c are considered variable. Note that f_c can be, for example, the time-varying rotational frequency f_r. The theoretical stator current analysis during transients, however, is identical to the steady state if relatively slow frequency variations are considered.

Under a mechanical fault, the load torque as a function of time is assumed to be described by a constant component Γ_const and an additional component varying at the fault characteristic frequency f_c. The first term of the variable component Fourier series is a cosine at frequency f_c. For the sake of clarity, higher order terms are neglected in the following and only the fundamental term is considered. The load torque can therefore be described by:

$$\Gamma_\mathrm{load}(t) = \Gamma_\mathrm{const} + \Gamma_\mathrm{c}\cos(\omega_\mathrm{c}t) \tag{1}$$

where Γ_c is the amplitude of the load torque oscillation and $\omega_\mathrm{c} = 2\pi f_\mathrm{c}$.

Considering the mechanical equation of the machine, the oscillating load torque leads to periodic oscillations at f_c of the mechanical rotor speed. The consequence is an oscillation at the same frequency on the mechanical rotor position. If the fundamental rotor MMF is expressed in the stator reference frame by using the transformation between the two reference frames, the oscillating mechanical rotor position produces an oscillating rotor MMF $F_\mathrm{r}(\theta,t)$ that can be written as [6]:

$$F_\mathrm{r}(\theta,t) = F_\mathrm{r}\cos\left(p\theta - \omega_\mathrm{s}t - \beta'\cos(\omega_\mathrm{c}t)\right) \tag{2}$$

with

$$\beta' = p\frac{\Gamma_\mathrm{c}}{J\omega_\mathrm{c}^2} \tag{3}$$

where p is the pole pair number, J the total inertia and $\omega_\mathrm{s} = 2\pi f_\mathrm{s}$. The fault effect on the rotor MMF can be seen as a sinusoidal PM at the characteristic fault frequency.

The stator MMF $F_\mathrm{s}(\theta,t)$ is not affected if secondary armature reactions are neglected. Thus, it takes the same expression as in the healthy case

$$F_\mathrm{s}(\theta,t) = F_\mathrm{s}\cos(p\theta - \omega_\mathrm{s}t - \varphi_\mathrm{s}) \tag{4}$$

where φ_s denotes the initial phase angle between rotor and stator MMF.

The total magnetic flux density is obtained by the multiplication of the total MMF with the airgap permeance, which is assumed constant. The induced voltage in a machine winding is related to the magnetic airgap field so that the PM is preserved. Consequently, a mechanical load fault leads to the following stator current expression (for an arbitrary machine phase):

$$\begin{aligned} i(t) &= i_\mathrm{st}(t) + i_\mathrm{rt}(t) \\ &= I_\mathrm{st}\sin\left[\omega_\mathrm{s}(t)t + \varphi_\mathrm{s}\right] \\ &\quad + I_\mathrm{rt}\sin\left[\omega_\mathrm{s}(t)t + \beta\cos\left(\omega_\mathrm{c}(t)t\right)\right] \end{aligned} \tag{5}$$

$i_\mathrm{st}(t)$ and $i_\mathrm{rt}(t)$ denote the stator current components resulting from the stator and rotor MMF. The amplitudes I_st and I_rt are expected to be quasi-constant. β is the PM index that is proportional to $\Gamma_\mathrm{c}/\omega_\mathrm{c}^2$. The healthy case is obtained when $\beta = 0$.

For the sake of simplicity, the time harmonics of rotor MMF and the nonuniform airgap permeance have not been considered. However, the harmonics of supply frequency f_s and the rotor slot harmonics theoretically show the same PM as the fundamental stator current component.

III. Time–Frequency Signal Processing

The time-varying supply frequencies in variable speed drives lead to nonstationary signals that require advanced signal processing methods for analysis. Traditional spectral estimation methods based on the FFT can no longer be applied. One possible solution for signal analysis is the use of time–frequency distributions [11], [12] that represent the signal energy with respect to time and frequency.

A multitude of possible time–frequency distributions exists with different properties. A simple method is the spectrogram, which is equivalent to the squared short-time Fourier transform (STFT). It was applied in [13] to induction motor fault diagnosis. The WD, proposed by Wigner in [14] and applied to signal processing by Ville [15], is a quadratic time–frequency distribution which provides high resolution. It is particularly

adapted to the analysis of linearly varying frequencies, as can often be found in electrical drives.

A. Wigner Distribution (WD)

The WD is defined as follows:

$$W_x(t,f) = \int_{-\infty}^{+\infty} x\left(t+\frac{\tau}{2}\right) x^*\left(t-\frac{\tau}{2}\right) e^{-j2\pi f\tau} d\tau \quad (6)$$

where x^* denotes the complex conjugate of x. This formula can be seen as the Fourier transform (FT) of a kernel $K_x(\tau,t)$ with respect to the delay variable τ. The kernel is similar to an instantaneous autocorrelation function

$$K_x(\tau,t) = x\left(t+\frac{\tau}{2}\right) x^*\left(t-\frac{\tau}{2}\right). \quad (7)$$

An interesting property of the WD is its perfect concentration on the instantaneous frequency in the case of a linear frequency modulation. However, other types of modulations (e.g., in our case sinusoidal PMs) produce so-called inner interference terms in the distribution [16]. It will be shown that the interferences may however be used for detection purposes.

An important drawback of the distribution is its nonlinearity due to the quadratic nature. When the sum of two signals is considered, so-called outer interference terms appear in the distribution at time instants or frequencies where there should not be any signal energy [16]. If harmonic signals such as the stator current are analyzed, appropriate filtering is necessary to remove higher harmonics. Furthermore, the WD should not be calculated on real signals but rather on the associated analytical signal obtained through the Hilbert transform [12]. This avoids interferences between positive and negative frequencies.

In practice, the Pseudo WD (PWD), a smoothed version of the WD, is often used. PWD is defined as follows [12]:

$$\mathrm{PW}_x(t,f) = \int_{-\infty}^{+\infty} p(\tau) x\left(t+\frac{\tau}{2}\right) x^*\left(t-\frac{\tau}{2}\right) e^{-j2\pi f\tau} d\tau \quad (8)$$

where $p(\tau)$ is the smoothing window which reduces the amplitudes of the interference terms. Since the window is only a function of τ, the smoothing takes place in the direction of frequency and not in time. Therefore, the time resolution is not degraded by this type of smoothing.

B. WD of Stator Current in Steady State

To obtain the WD of the stator current according to (5) with constant supply and fault frequency, the WD of an analytical phase modulated signal $i_{\mathrm{rt}}(t)$ will first be calculated with

$$i_{\mathrm{rt}}(t) = I_{\mathrm{rt}} \exp j\left[\omega_{\mathrm{s}} t + \beta\cos(\omega_{\mathrm{c}} t)\right]. \quad (9)$$

The kernel for this signal can be written as follows:

$$\begin{aligned} K_{i_{\mathrm{rt}}}(t,\tau) &= i_{\mathrm{rt}}\left(t+\frac{\tau}{2}\right) i_{\mathrm{rt}}^*\left(t-\frac{\tau}{2}\right) \\ &= I_{\mathrm{rt}}^2 \exp j\left\{\omega_{\mathrm{s}}\tau - 2\beta\sin(\omega_{\mathrm{c}} t)\sin\left(\frac{\omega_{\mathrm{c}}}{2}\tau\right)\right\}. \end{aligned} \quad (10)$$

The WD is obtained as the FT of the kernel with respect to the delay τ

$$\begin{aligned} W_{i_{\mathrm{rt}}}(t,f) &= \mathrm{FT}_\tau\left\{K_{i_{\mathrm{rt}}}(t,\tau)\right\} \\ &= I_{\mathrm{rt}}^2 \mathrm{FT}_\tau\left\{\exp j(\omega_{\mathrm{s}}\tau)\right\} \\ &\quad * \mathrm{FT}_\tau\left\{\exp j\left[-2\beta\sin(\omega_{\mathrm{c}} t)\sin\left(\frac{\omega_{\mathrm{c}}}{2}\tau\right)\right]\right\} \end{aligned} \quad (11)$$

where $*$ denotes the convolution product. The FT of the second term may be calculated in analogy to the FT of a pure PM signal using the Jacobi–Anger expansion [18] given by

$$e^{j\gamma\sin\theta} = \sum_{n=-\infty}^{+\infty} J_n(\gamma) e^{jn\theta} \quad (12)$$

where J_n denotes the n-th order Bessel function of the first kind.

The second term in (11) can therefore be developed into a Fourier series which allows a simple calculation of its FT

$$\begin{aligned} W_{i_{\mathrm{rt}}}(t,f) &= I_{\mathrm{rt}}^2 \delta(f-f_{\mathrm{s}}) \\ &\quad * \mathrm{FT}_\tau\left\{\sum_{n=-\infty}^{+\infty} J_n\left(-2\beta\sin(\omega_{\mathrm{c}} t)\right) e^{jn\frac{\omega_{\mathrm{c}}}{2}\tau}\right\} \\ &= I_{\mathrm{rt}}^2 \sum_{n=-\infty}^{+\infty} J_n\left(-2\beta\sin(\omega_{\mathrm{c}} t)\right) \delta\left(f-f_{\mathrm{s}}-n\frac{f_{\mathrm{c}}}{2}\right) \end{aligned} \quad (13)$$

where $\delta(f)$ is the Dirac delta function. For small modulation indices β, the Bessel functions of order $n \geq 2$ are very small and may be neglected (narrowband approximation from communication theory)

$$\begin{aligned} W_{i_{\mathrm{rt}}}(t,f) &\approx I_{\mathrm{rt}}^2 J_0\left(\gamma(t)\right)\delta(f-f_{\mathrm{s}}) \\ &\quad + I_{\mathrm{rt}}^2 J_1\left(\gamma(t)\right)\delta\left(f-f_{\mathrm{s}}-\frac{f_{\mathrm{c}}}{2}\right) \\ &\quad - I_{\mathrm{rt}}^2 J_1\left(\gamma(t)\right)\delta\left(f-f_{\mathrm{s}}+\frac{f_{\mathrm{c}}}{2}\right) \end{aligned} \quad (14)$$

with $\gamma(t) = -2\beta\sin(\omega_{\mathrm{c}} t)$. The WD of the considered pure phase modulated signal is therefore a central frequency at f_{s} with sidebands at $f_{\mathrm{s}} \pm f_{\mathrm{c}}/2$. All the components have time-varying amplitudes at frequency f_{c}. It is important to note that the lower sideband has the opposite sign to the upper sideband.

The Bessel functions $J_0(\gamma(t))$ and $J_1(\gamma(t))$ can be approximated for small arguments γ by [18]

$$J_0\left(\gamma(t)\right) \approx 1 \quad (15)$$

$$J_1\left(\gamma(t)\right) \approx \frac{\gamma}{2} = -\beta\sin(\omega_{\mathrm{c}} t). \quad (16)$$

As the stator current signal is the sum of two components, a phase modulated signal and a pure frequency [see (5)], its WD

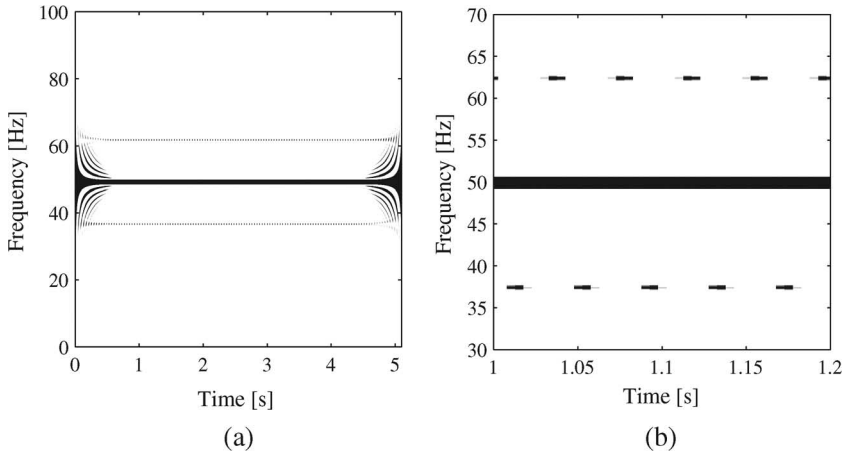

Fig. 1. PWD of simulated steady state PM signal. (a) Global view. (b) Detail.

must be calculated according to the following expression for the sum of two signals $x + y$ [12]:

$$W_{x+y}(t,f) = W_x(t,f) + W_y(t,f) + 2\mathrm{Re}\left\{W_{xy}(t,f)\right\} \tag{17}$$

with

$$W_{xy}(t,f) = \int_{-\infty}^{+\infty} x\left(t+\frac{\tau}{2}\right) y^*\left(t-\frac{\tau}{2}\right) e^{-j2\pi f\tau} d\tau. \tag{18}$$

The WD of the pure frequency $i_{\mathrm{st}}(t) = I_{\mathrm{st}}\sin(\omega_{\mathrm{s}}t + \varphi_{\mathrm{s}})$ [first term of (5)] is given by $I_{\mathrm{st}}^2\delta(f - f_{\mathrm{s}})$. A detailed calculation of the cross terms $W_{i_{\mathrm{st}}i_{\mathrm{rt}}}$ shows that they are of small amplitude and do not introduce new frequency components. Thus, the cross terms may be neglected in this case and the following approximate expression is obtained for the WD of (5):

$$\begin{aligned} W_{i_{\mathrm{st}}+i_{\mathrm{rt}}}(t,f) \approx\ & \left(I_{\mathrm{rt}}^2 + I_{\mathrm{st}}^2\right)\delta(f - f_{\mathrm{s}}) \\ & - I_{\mathrm{rt}}^2\beta\sin(\omega_{\mathrm{c}}t)\delta\left(f - f_{\mathrm{s}} - \frac{f_{\mathrm{c}}}{2}\right) \\ & + I_{\mathrm{rt}}^2\beta\sin(\omega_{\mathrm{c}}t)\delta\left(f - f_{\mathrm{s}} + \frac{f_{\mathrm{c}}}{2}\right). \end{aligned} \tag{19}$$

In contrast to the pure phase modulated signal, the constant component I_{st} is present at the fundamental frequency. The fault characteristic signature is conserved.

These considerations are illustrated in Fig. 1, where a detail of the PWD of the PM signal $s_1(t)$ is displayed. The plot is in logarithmic scale and only positive values are displayed. $s_1(t)$ is the sum of a pure sine and a sinusoidal PM signal

$$s_1(t) = \cos\left(2\pi f_{\mathrm{s}}t + \pi/8\right) + \cos\left(2\pi f_{\mathrm{s}}t + \beta\cos(2\pi f_{\mathrm{c}}t)\right) \tag{20}$$

with $f_{\mathrm{s}} = 50$ Hz, $f_{\mathrm{c}} = 25$ Hz, $\beta = 0.05$ and sampling frequency $= 200$ Hz. The PWD of $s_1(t)$ clearly shows the theoretically predicted signature: a strong component is visible at f_{s} with sidebands at $f_{\mathrm{s}} \pm f_{\mathrm{c}}/2$. The sideband amplitudes are time-varying at modulation frequency f_{c}. Furthermore, the two sidebands have opposed amplitudes at a given time instant. An additional 3-D plot in the frequency range of the upper sideband (see Fig. 2) confirms the oscillating nature with positive and negative PWD values. The relative sideband amplitude with respect to the fundamental is $6/246 \approx 0.025$, which corresponds to $I_{\mathrm{rt}}^2\beta/(I_{\mathrm{rt}}^2 + I_{\mathrm{st}}^2)$ with the chosen values. The oscillation frequency is $f_{\mathrm{c}} = 25$ Hz.

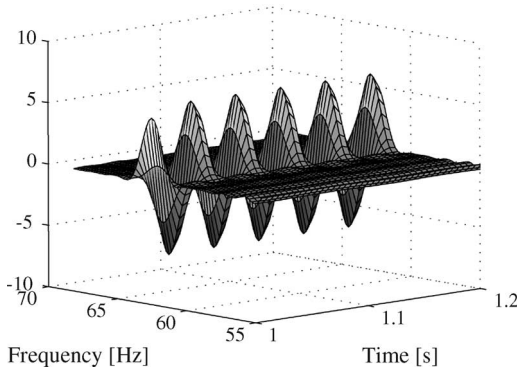

Fig. 2. Three-dimensional PWD representation of simulated steady state PM signal in the frequency range of the upper sideband.

C. WD of Transient Stator Current

During speed transients, the supply and fault frequencies are time-varying. For the calculation of the WD of a transient stator current under fault, these frequencies are modeled as linear functions of time

$$f_{\mathrm{s}}(t) = \alpha_{\mathrm{s}} + \beta_{\mathrm{s}}t \tag{21}$$

$$f_{\mathrm{c}}(t) = \alpha_{\mathrm{c}} + \beta_{\mathrm{c}}t. \tag{22}$$

The instantaneous frequencies $f_{\mathrm{i,s}}(t)$ and $f_{\mathrm{i,c}}(t)$ of a sinusoidal signal $\sin[2\pi f_{\mathrm{s}}(t)t]$ (respectively $\sin[2\pi f_{\mathrm{c}}(t)t]$) would be (see [12])

$$f_{\mathrm{i,s}}(t) = \alpha_{\mathrm{s}} + 2\beta_{\mathrm{s}}t \tag{23}$$

$$f_{\mathrm{i,c}}(t) = \alpha_{\mathrm{c}} + 2\beta_{\mathrm{c}}t. \tag{24}$$

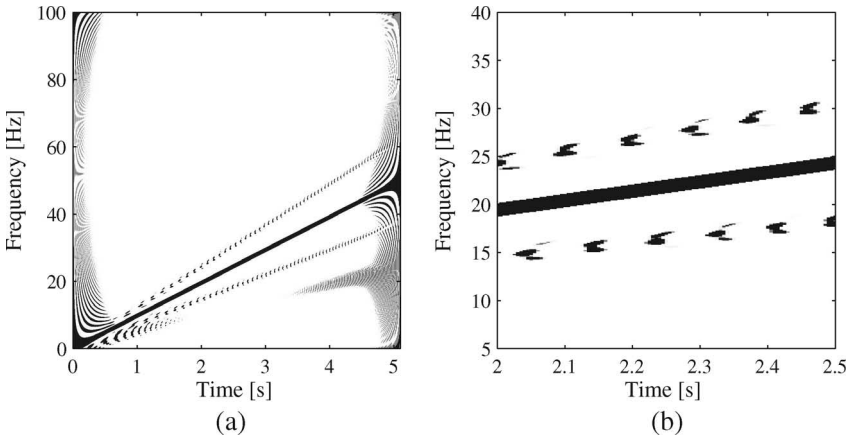

Fig. 3. PWD of simulated transient PM signal. (a) Global view. (b) Detail.

Using similar approximations in the precedent, the WD of a transient current signal becomes

$$\begin{aligned} W_i(t,f) \approx\ & \left(I_{\mathrm{rt}}^2 + I_{\mathrm{st}}^2\right)\delta\left(f-(\alpha_{\mathrm{s}}+2\beta_{\mathrm{s}}t)\right) \\ & - I_{\mathrm{rt}}^2\beta(t)\sin\left(\omega_{\mathrm{c}}(t)t\right) \\ & \times\delta\left(f-(\alpha_{\mathrm{s}}+2\beta_{\mathrm{s}}t)-\left(\frac{\alpha_{\mathrm{c}}}{2}+\beta_{\mathrm{c}}t\right)\right) \\ & + I_{\mathrm{rt}}^2\beta(t)\sin\left(\omega_{\mathrm{c}}(t)t\right) \\ & \times\delta\left(f-(\alpha_{\mathrm{s}}+2\beta_{\mathrm{s}}t)+\left(\frac{\alpha_{\mathrm{c}}}{2}+\beta_{\mathrm{c}}t\right)\right) \end{aligned} \quad (25)$$

with $\omega_{\mathrm{c}}(t) = 2\pi f_{\mathrm{c}}(t)t$. The central component of the WD is now time-varying according to the instantaneous frequency law $f_{\mathrm{i,s}}(t)$ of the fundamental stator current component. The sidebands are located at $f_{\mathrm{i,s}}(t) \pm f_{\mathrm{i,c}}(t)/2$ analogous to the stationary case. Their opposed amplitudes are also time-varying. It should also be noted that β is no longer constant during transients, as it is proportional to $1/\omega_{\mathrm{c}}^2$.

For illustration of the stator current signature in the transient case, consider Fig. 3 where the PWD of a transient signal is displayed. The signal is identical to $s_1(t)$, but with linearly varying supply and fault frequencies f_{s} and f_{c} to consider a case similar to a motor start-up. The modulation index β is kept constant in this example. The theoretically calculated signature is clearly visible. However, stronger interferences due to the time-varying frequencies can also be recognized.

D. Comparison of STFT and WD

This section compares the PWD to the STFT and justifies its use. Jones and Parks compared in [17] the resolution of the STFT to the WD and smoothed WDs. They stated that the STFT yields a better resolution than the WD for multicomponent signals with significant frequency modulation if matched windows are used. On the contrary, they found that the PWD resolves multicomponent signals without modulation better than the STFT.

In our application, the signals are mono-component phase-modulated signals with linearly varying carrier frequencies and small modulation indices. *A priori* knowledge is not available since the frequencies can be stationary or vary with different sweep rates. This signifies that matched windows cannot be used. Moreover, the STFT cannot provide a high resolution in time and frequency due to the Heisenberg–Gabor uncertainty principle [12]. Although good frequency resolution requires long windows, this may lead to a high degree of nonstationarity of the windowed signal if the frequency sweep rate is high. The consequence is broad peaks which might overlap and cover the sidebands. Moreover, their amplitude depends on the frequency sweep rate.

The PWD offers a good compromise between resolution and interference suppression. Time resolution is equivalent to the WD, whereas slight smoothing in the frequency direction suppresses some interference terms. The characteristic PM interference structure is preserved and can be used for detection purposes. The peak amplitudes and the resolution do not depend on the frequency sweep rate. Numerical calculations with simulated signals confirm the difficulty of finding an optimal window length for the STFT under varying frequency sweep rates. In conclusion, the performance with the PWD was found to be superior and thus, it is employed in this paper.

IV. DSP Implementation

Two different detection algorithms based on stator current time–frequency analysis have been implemented on a DSP (see Section IV-C). The DSP is a low-cost Analog Devices ADSP-21161 (21161N EZ-Kit lite), mainly designed for audio applications. The inputs include antialiasing filters and 24-bit AD-converters with a minimum sampling rate of 48 kHz. As the fault signatures appear around the fundamental supply frequency of 50 Hz, a lower sampling rate would be advantageous but cannot be realized with this hardware. Therefore, a preprocessing stage with filtering and downsampling is implemented numerically before calculation of the WD.

A. Preprocessing

1) Downsampling: The stator current is sampled at 48 kHz. However, relevant fault frequencies with the two pole pair

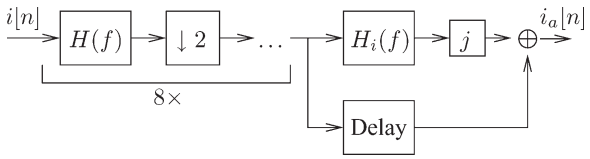

Fig. 4. Preprocessing of stator current signal: low-pass filter $H(f)$, decimation and Hilbert filter $H_i(f)$.

machines are at a maximum frequency 1.5 times the supply frequency f_s, which leads approximately to 75 Hz for the considered machine in nominal conditions. As a consequence, a real-time downsampling stage is implemented to decrease the sampling frequency by a factor $2^8 = 256$, i.e., the new sampling frequency is 187.5 Hz. The implementation of a single low-pass filter with normalized cutoff frequency $1/(2 \cdot 256)$ followed by a 256-fold decimator (takes one sample out of 256) would require a high filter order and a significant amount of memory for storage. It is more efficient to implement a scheme as depicted in Fig. 4 with eight decimation stages in cascade, each including the same filter $H(f)$ with a normalized cutoff frequency 0.25 followed by a two-fold decimator. Main benefits are a low global order, small time delay and low computational cost.

More precisely, the implemented low-pass filter $H(f)$ is an elliptic infinite impulse response (IIR) filter of order 14. Its normalized cutoff frequency at -3 dB is 0.227 so that after the last downsampling stage, frequencies between 0 and 85.03 Hz can be analyzed without significant attenuation.

2) Hilbert Filtering: The WD should be calculated on the complex, analytical current signal to avoid interferences [12]. The analytical current signal $i_\mathrm{a}[n]$ is obtained from the real current signal $i[n]$ by means of the Hilbert transform $H\{.\}$ according to

$$i_\mathrm{a}[n] = i[n] + jH\left\{i[n]\right\}. \tag{26}$$

The Hilbert transform is realized using a Hilbert filter with the following frequency response:

$$H_i(f) = \begin{cases} -j & \text{for } 0 \le f \le \frac{1}{2} \\ j & \text{for } -\frac{1}{2} \le f < 0. \end{cases} \tag{27}$$

Its impulse response $h_i[n]$ is

$$h_i[n] = \frac{2\sin^2(\pi n/2)}{\pi n} = \begin{cases} 0 & \text{if } n \text{ is even} \\ \frac{2}{\pi n} & \text{if } n \text{ is odd.} \end{cases} \tag{28}$$

In practice, the Hilbert filter is implemented as an IIR filter of order $N_i = 257$. To observe causality, the symmetric impulse response must be shifted by $(N_i - 1)/2$. The filter output is therefore delayed by 128 samples corresponding to 0.688 s. The analytical signal $i_\mathrm{a}[n]$ is obtained by multiplication of the filter output with j and addition of the delayed real signal $i[n]$ (see Fig. 4).

B. Discrete Implementation of the WD

The discrete WD $\mathrm{DWD}_x[n, m]$ of a signal $x[n]$ with length N can be calculated according to the following formula [12]:

$$\mathrm{DWD}_x[n,m] = 2\sum_{k=-(N-1)}^{N-1} p[k]x[n+k]x^*[n-k]e^{-j4\pi mk/N} \tag{29}$$

where $p[k]$ is a window function. This expression can be efficiently implemented using an FFT algorithm (see [19] for a sample algorithm). In this paper, the DWD is calculated on data records with length $N = 512$. The window function $p[k]$ is a 127 point Hamming window.

The result of the calculation would be a (512 $\times$ 512) matrix requiring a considerable amount of memory for storage. However, the DWD can be calculated for each time bin n independently; the fault indicator can be directly derived for this time bin. This offers an advantage in the elimination of the need for storage of the complete DWD, and only the fault indicator is retained.

C. Fault Indicators

Two fault indicators based on the WD (WD1 and WD2) are proposed [20]. For comparison with traditional techniques, the results obtained with a spectrum-based indicator are also presented in steady-state operation. All the fault indicators are calculated on data records of length 512 samples after downsampling. As soon as one data buffer of length 512 is complete, the fault indicator is calculated while the arriving samples are written to a second buffer. The calculation of the indicator must therefore take less than 2.73 s, which is respected in all the cases.

1) Spectrum-Based Indicator: The magnitude of the FT of the phase-modulated stator current according to (5) is approximately (for small β [6])

$$|I(f)| \approx (I_\mathrm{st} + I_\mathrm{rt})\delta(f - f_\mathrm{s}) + I_\mathrm{rt}\frac{\beta}{2}\delta\left(f - (f_\mathrm{s} \pm f_\mathrm{r})\right) \tag{30}$$

where the fault frequency is supposed to be f_r.

The algorithm that calculates the spectrum-based fault indicator on a given buffer is the following.

1) Zero-padding of initial data record up to 1024 samples.
2) Discrete FT uses a Hanning window.
3) Search of the maximum absolute value of the FT I_m, corresponding to the supply frequency f_s.
4) Search of maxima I_1 and I_2 in intervals $[f_\mathrm{s} - f_\mathrm{s}/p, f_\mathrm{s} - 0.9f_\mathrm{s}/p]$ and $[f_\mathrm{s} + 0.9f_\mathrm{s}/p, f_\mathrm{s} + f_\mathrm{s}/p]$. The rotational frequency f_r is supposed to vary within these bounds under different load conditions.
5) The spectrum-based indicator is then given by $(I_1 + I_2)/I_m$.

The normalization with respect to the fundamental amplitude I_m reduces the dependence of the indicator on the machine load level.

2) Indicator WD1: The first indicator WD1 analyzes the energy in a region around the characteristic fault signature at

$f_s \pm f_r/2$ in the PWD. The rotational frequency is supposed to vary between $0.9f_s/p$ and f_s/p as before. The fault indicator is only calculated for time bins $n = 64$ to 448 to avoid border regions with strong interferences. The detailed steps are as follows:

1) For $n = 64$ to 448.
   a) Calculate DWD$[n, m]$.
   b) Determine frequency bin m_A belonging to strongest absolute value A (supply frequency).
   c) Calculate frequency bins corresponding to intervals $I_1 = [(1 + 0.9/2p)m_A, (1 + 1/2p)m_A]$ and $I_2 = [(1 - 1/2p)m_A, (1 - 0.9/2p)m_A]$.
   d) A_1 and A_2 are the sums of the absolute value of DWD$[n, m]$ in the intervals I_1 and I_2.
   e) Normalization: WD1$[n] = (A_1 + A_2)/A$.
2) The fault indicator WD1 is the sum of all the WD1$[n]$.

The normalization of the energy with respect to the fundamental is done for each time bin. Similar to the spectrum-based indicator, it improves the indicator behavior under varying load levels. Since the fault signature is oscillating with positive and negative values in the PWD, absolute values are considered.

3) Indicator WD2: For the second indicator WD2, two pseudosignals $s_1[n]$ and $s_2[n]$ are synthesized by recording at each time instant the highest absolute value of the PWD in intervals I_1 and I_2. They represent the oscillating fault signature in the upper and lower sidebands. According to (19), these signals theoretically oscillate at the fault frequency f_r and their amplitude is proportional to β. Once recorded, the amplitudes of $s_1[n]$ and $s_2[n]$ have to be extracted. One possibility is spectrum analysis in an interval that takes into account possible values of f_r. The interval is calculated as a function of the minimum and maximum estimated supply frequencies for the considered data record. If the signals are highly nonstationary, instantaneous amplitude analysis of the corresponding analytical signals is preferable. However, the spectrum-based method is used further in this paper due to relatively limited variations of f_r during one data record.

1) For $n = 64$ to 448.
   a) Calculate DWD$[n, m]$.
   b) Determine fundamental amplitude A and the intervals I_1 and I_2 as with WD1.
   c) Find maximum absolute value of DWD$[n, m]$ in I_1 and I_2 and retain the corresponding signed values A_1 and A_2.
   d) Synthesis of the pseudosignals including a normalization: $s_1[n] = A_1/A$, $s_2[n] = A_2/A$.
2) Calculate the minimum and maximum possible values of f_r based on the minimum and maximum supply frequencies.
3) Discrete FT of s_1 and s_2 using 512 points (zero-padding) and a Hanning window.
4) Derivation of energies E_1 and E_2 in the interval $[f_{r,\min}, f_{r,\max}]$.
5) WD2 is the sum of E_1 and E_2.

This second indicator is more complex to calculate, but theoretically, it should be more accurate than WD1. Since WD1 takes the absolute values of the PWD in a time–frequency region, it can be influenced by noise or oscillating signatures at other frequencies. The indicator WD2 is only dependent on the oscillating energy at certain frequencies, which makes it insensitive to such phenomena.

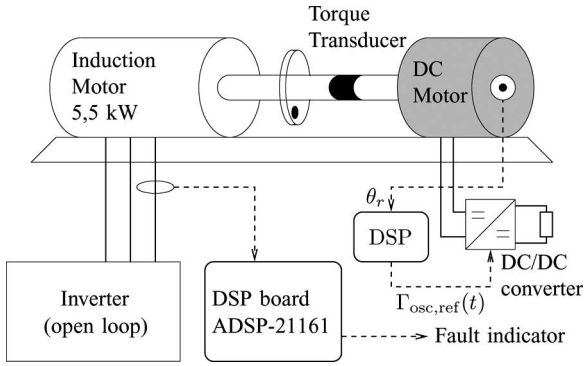

Fig. 5. Scheme of the experimental setup.

V. Experimental Results

A. Description of Experimental Set-Up

Tests have been conducted on an experimental set-up with a three phase, 400 V, 50 Hz, 5.5 kW Leroy Somer induction machine (see Fig. 5). The motor has two pole pairs and a nominal torque of about 36 N · m. The machine is supplied by a standard industrial inverter operating in open-loop condition with a constant voltage to frequency ratio. The load is a DC motor with separate, constant excitation connected to a resistor through a DC/DC converter. Measured quantities for off-line analysis are the three terminal voltages, three line currents, speed and load torque. All the signals are acquired at 25 kHz by a 24-bit data acquisition system. Further signal processing is done on a standard desktop PC using Matlab. In parallel, one line current signal is fed into the DSP for on-line analysis.

The load torque oscillations are produced as follows: a DC/DC converter (Buck) is used to control the DC motor armature current. Thus, a constant load torque with a small additional oscillating component can be introduced. The reference signal for the oscillation is generated by the DSP that receives position information from an incremental encoder. However, the reference is generated independently from stator current processing, and neither the position signal nor a speed measurement is used for the stator current on-line analysis. The oscillating torque component Γ_{osc} is synchronous with respect to the mechanical rotor position θ_r and takes the following form:

$$\Gamma_{\mathrm{osc}}(t) = \Gamma_c \cos\left(\theta_r(t) + \varphi_r\right). \tag{31}$$

To study realistic load torque oscillations introduced by a fault, load imbalance is considered. It can be created by fixing a mass eccentrically on a disc placed on the shaft. In the following test, a mass of $m = 77$ g has been fixed at a distance of $r = 75$ mm from the center. The mass has two effects: first, the weight leads to a load torque oscillation of amplitude $\Gamma_c = mgr$ according to (31). Second, a centrifugal force acts on the shaft. This may result in an increasing level of dynamic eccentricity depending on bearing tolerances and shaft stiffness.

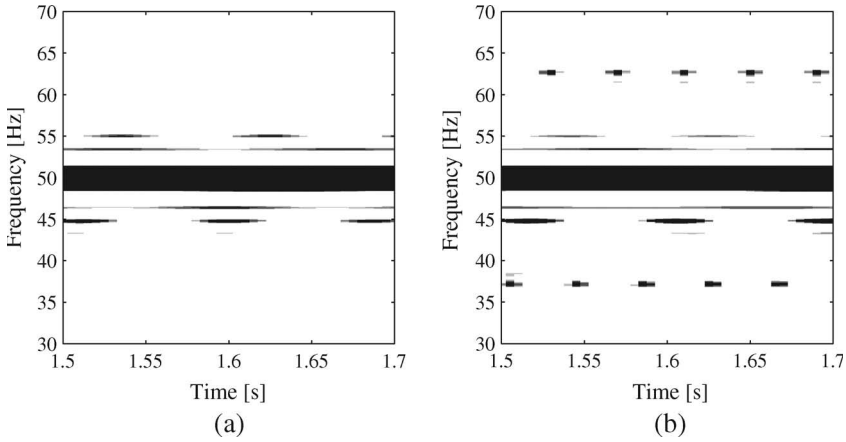

Fig. 6. PWD of healthy and faulty stator current in steady state at 50% load. (a) Healthy. (b) Faulty.

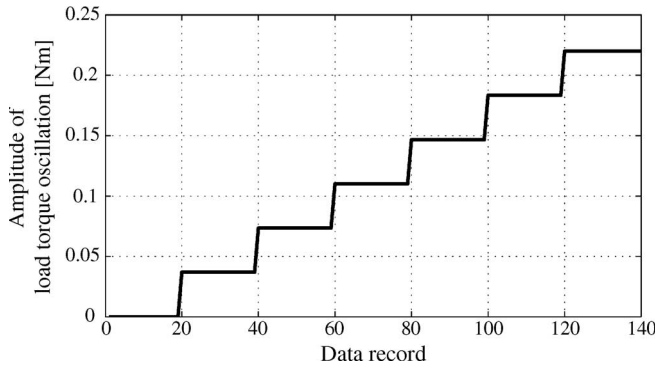

Fig. 7. Considered fault profile: Load torque oscillation amplitude Γ_c versus data records.

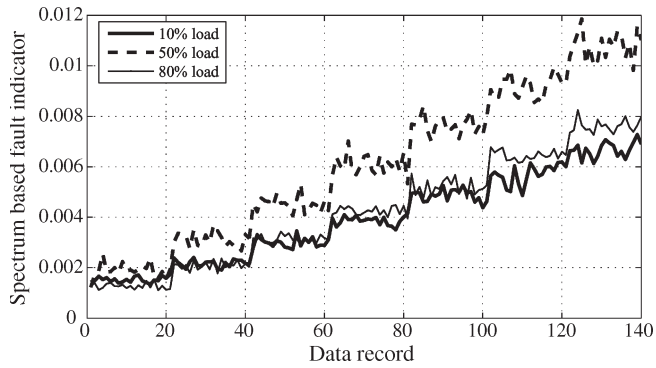

Fig. 8. Spectrum-based fault indicator versus data records.

B. Steady-State Results

1) Off-Line Analysis: The stator current has been recorded and processed off-line to study the fault effects on the stator current spectrum and the WD. The spectral analysis reveals a rise at frequencies $f_s \pm f_r$ with magnitudes related to the fault level as expected. Details of the WD are shown in Fig. 6 for the healthy and faulty motor stator current at 50% load. The load torque oscillation amplitude in the faulty case was $\Gamma_c = 0.22$ N · m. The theoretically calculated interference signature is present on the displayed WD of the faulty current signal at $f_s \pm f_r/2 \approx 50 \pm 12.5$ Hz, whereas the WD of the healthy stator current does not show any energy at the considered frequencies. However, other interferences are visible at frequencies close to the fundamental. It should also be noted that a certain threshold for amplitude visualization in the WD was chosen. This signifies that certain interferences and components of small amplitude, e.g., those resulting from natural eccentricity, are not displayed.

2) On-Line Analysis: The load torque oscillations in steady state are imposed according to the fault profile displayed in Fig. 7. During the first 20 data records (corresponding to 55 s), the DC machine armature current reference contains no oscillating component. The amplitude of the oscillating component then increases after each 20 data records to obtain 6 fault levels from $\Gamma_c = 0.03$ to 0.22 N · m (measured values). Note that for the lowest fault level, Γ_c is only about 0.1% of the nominal motor torque.

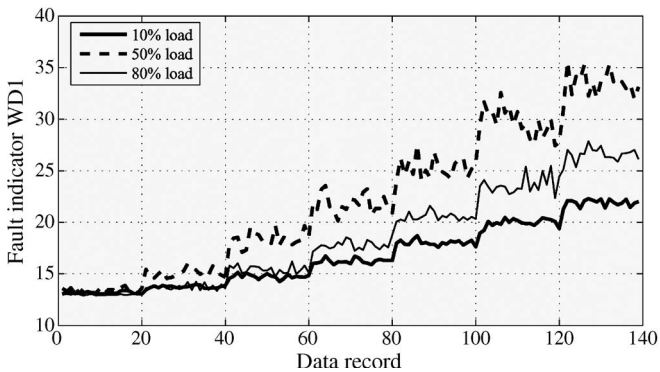

Fig. 9. Fault indicator WD1 versus data records.

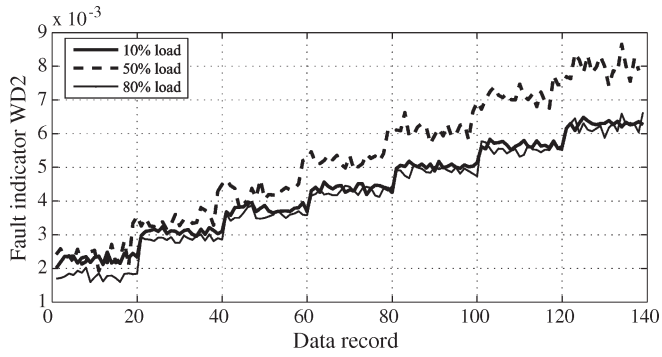

Fig. 10. Fault indicator WD2 versus data records.

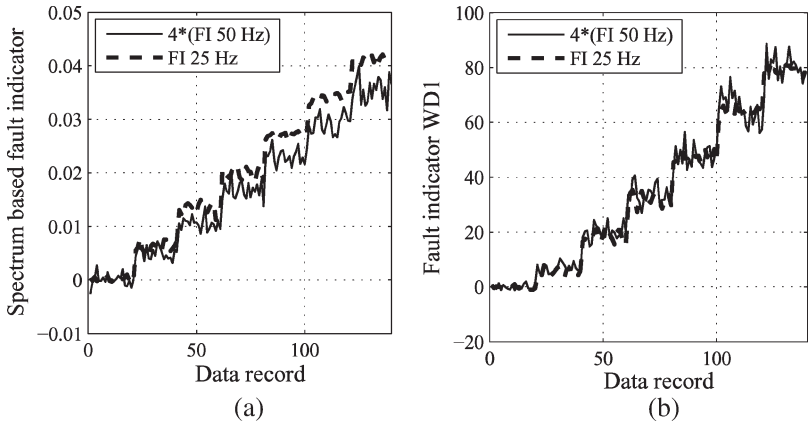

Fig. 11. Fault indicators at 25 and 50 Hz supply frequency versus data records. (a) Spectrum-based fault indicator. (b) Fault indicator WD1.

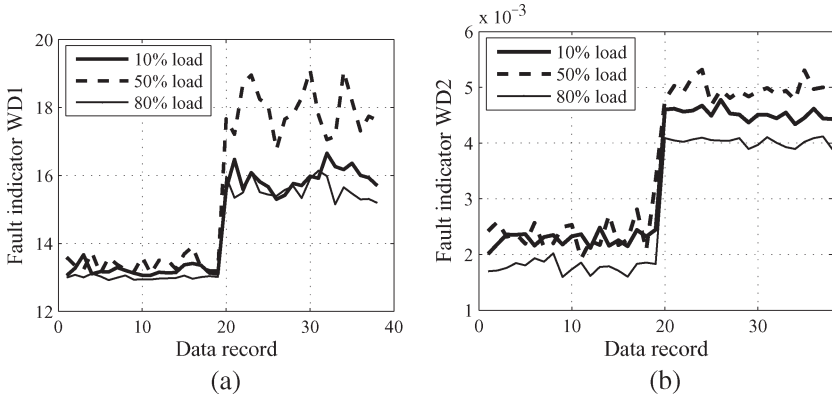

Fig. 12. Fault indicators WD1 and WD2 in healthy state (data records 1 to 19) and with load unbalance (data records 20 to 40). (a) Fault indicator WD1. (b) Fault indicator WD2.

The results obtained with the spectrum-based fault indicator are shown in Fig. 8 for the nominal supply frequency and three different load levels. The indicator evolves approximately linearly with respect to the amplitude of the load torque oscillation. This is the case for all average load levels. Even the smallest torque oscillation of only 0.1% of the nominal torque can still be detected. However, the evolution of the indicator is sensitive to the average load level. The indicator is higher with 50% load than with small load or 80% load. This can be explained by the normalization with respect to the fundamental stator current amplitude, which is $I_{\rm st} + I_{\rm rt}$. But the sideband amplitudes are $\beta I_{\rm rt}$, i.e., the correct normalization should only use the rotor current amplitude $I_{\rm rt}$, which is unfortunately not directly available. Nevertheless, it was observed that the proposed normalization improves the independence of the indicator with respect to load compared to no normalization at all.

The results obtained under the same test conditions with the two indicators based on the WD, WD1 and WD2, are displayed in Figs. 9 and 10. Both indicators show an approximately linear rise with respect to the amplitude of the load torque oscillation. The indicator WD2 seems more sensitive to the increase of $\Gamma_{\rm c}$ than WD1. A possible explanation is the more precise analysis with respect to the fault frequency in the case of WD2. WD1 is based on the total energy in the WD in a given frequency interval, whereas WD2 only considers the energy of pulsating components at fault frequency. It can also be noted that WD2 depends less on the average load level than WD1.

Additional tests at lower supply frequency were conducted to verify the fault indicator behavior at lower speed. The fault indicators are quantities that should represent the evolution of the PM modulation index β. Since β is proportional to $1/\omega_{\rm c}^2$ according to the theoretical development, the fault indicator should therefore show the same behavior. This was verified at supply frequency $f_{\rm s} = 25$ Hz, which leads approximately to half the fault frequency $f_{\rm c}$. The indicator should therefore be four times higher compared to $f_{\rm s} = 50$ Hz. Fig. 11 shows the spectrum-based fault indicator and WD1 for the two different supply frequencies. The healthy state of all the indicators was referenced to zero. The indicators at $f_{\rm s} = 50$ Hz were multiplied by four to allow the comparison. A good agreement between the indicators can be found, especially for WD1, which proves experimentally that $\beta \propto 1/\omega_{\rm c}^2$. The results with the indicator WD2 are not displayed, but are similar to those obtained with the spectrum-based indicator.

3) Load Imbalance: The three proposed fault detection schemes are tested with an unbalanced load. The small mass leads theoretically to a sinusoidal torque oscillation of amplitude 0.057 N · m. The results obtained with the WD-based fault indicators at $f_{\rm s} = 50$ Hz are displayed in Fig. 12. Both indicators clearly detect the fault under all tested load conditions. The magnitude of the indicators in the faulty case is

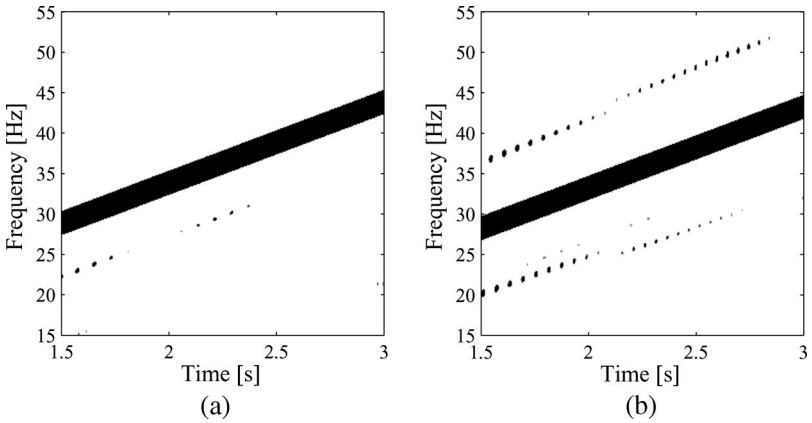

Fig. 13. PWD of healthy and faulty stator current during speed transient at 50% load. (a) Healthy. (b) Faulty.

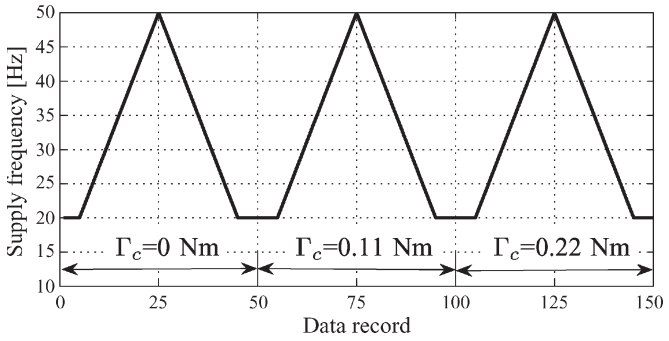

Fig. 14. Considered speed profile: Supply frequency f_s versus data records and corresponding torque oscillation amplitude.

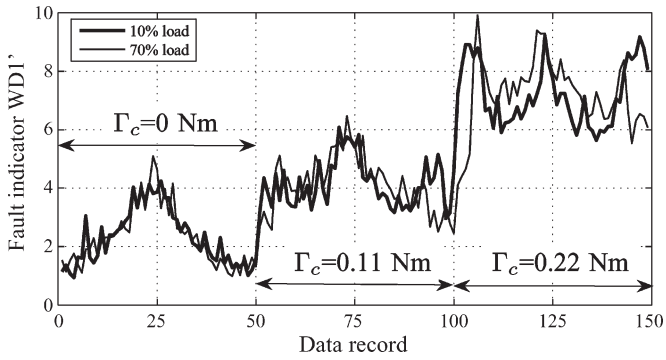

Fig. 15. Fault indicator WD1′ versus data records during speed transients.

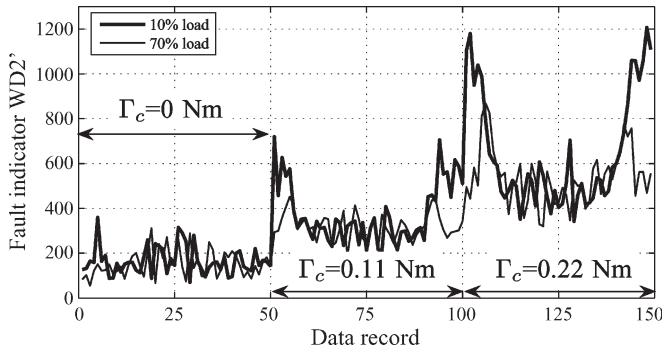

Fig. 16. Fault indicator WD2′ versus data records during speed transients.

comparable to the second or third fault level in the precedent tests, corresponding to values of Γ_c from 0.07 to 0.11 N · m. The values are higher than expected, possibly due to effects of the centrifugal force. As in the case of the load torque oscillations, WD2 is less dependent on the load level than WD1. Despite the indicator dependence on the load level, a simple detector using the same threshold for all load levels could be employed.

C. Results During Transient Operation

1) Off-Line Analysis: The stator current has been recorded during a motor start-up from 0 to 50 Hz supply frequency in 5 s. The WDs of the healthy and faulty stator current can be compared in Fig. 13 for 50% average load and $\Gamma_c = 0.22$ N · m. The expected interference signature is visible at $f_s \pm f_r/2$ in the faulty case.

2) On-Line Analysis: The algorithms used in the preceding part for steady-state current analysis are tested under motor operation at variable speed. One modification of the described algorithms is necessary for a correct operation: Until now, the algorithms have estimated a quantity directly proportional to the PM index β in (5). However, β depends on the fault characteristic frequency f_c that itself depends on f_r and f_s [see (3)]. Therefore, the obtained fault indicator with the precedent algorithms must be multiplied by f_c^2 to yield a result independent of speed. Since f_c and f_r are directly proportional to f_s, it is equivalent to multiplying the indicator with the estimated value of f_s. The modified indicators are denoted WD1′ and WD2′.

The speed profile used in the following tests is displayed in Fig. 14. During one speed cycle, the supply frequency f_s varies linearly from 20 to 50 Hz during 20 data records and back to 20 Hz in the same way. At the start and end of one cycle, f_s is constant during five data records. This speed cycle is repeated three times: first without a load torque oscillation, then with $\Gamma_c = 0.11$ N · m and $\Gamma_c = 0.22$ N · m. The lowest supply frequency is 20 Hz because of the DC machine voltage drop. Below this value, DC motor armature current control is no longer possible, and torque oscillations are not correctly produced.

Tests with the first fault indicator WD1′ gave the results displayed in Fig. 15 for two constant average load torques

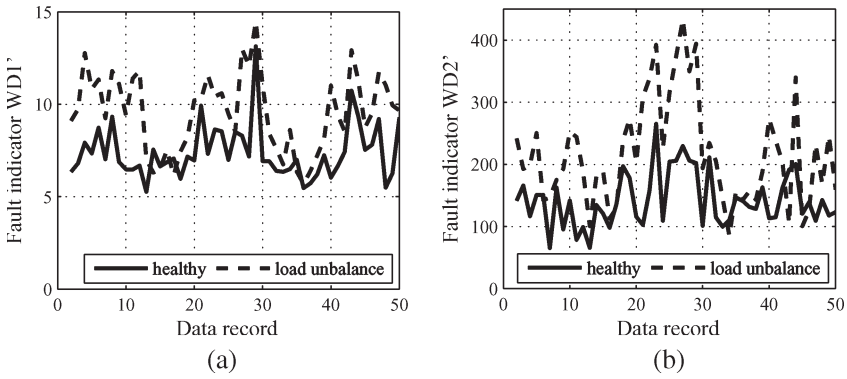

Fig. 17. Fault indicators WD1′ and WD2′ versus data records during speed transients with load unbalance. (a) WD1′. (b) WD2′.

corresponding to 10% and 70% load. During the first speed cycle without any oscillating torque, the indicator shows variations and is therefore still speed dependent with higher values at higher motor speed. When the first level of torque oscillation is applied from data record 50 onwards, the indicator jumps to a higher value. During the second speed cycle, the indicator value still depends on the speed, but relative variations between $f_s = 20$ Hz and $f_s = 50$ Hz are much smaller. The same behavior can be observed during the third speed cycle with a higher oscillating torque. It can be concluded from these tests that the fault indicator WD1′ still depends on speed, despite the previously mentioned indicator correction. A simple threshold cannot clearly distinguish between the healthy case and $\Gamma_c = 0.11$ N · m (0.3% of nominal torque). However, for a given speed or supply frequency, the fault indicator is always higher in the presence of torque oscillation. With stronger oscillations ($\Gamma_c = 0.22$ N · m or 0.6% of nominal torque), the discrimination is possible for all considered speeds.

The results obtained with the second indicator WD2′ are shown in Fig. 16 for the same two load levels. It can be noted that WD2′ is less varying during the first speed cycle compared to WD1′. The behavior during cycles with torque oscillation shows higher indicator values at low speed, whereas the indicator is approximately constant above a certain minimal supply frequency (about 30 Hz). It can further be observed that the relative variation of the mean indicator value between the healthy state and $\Gamma_c = 0.22$ N · m is smaller than with WD1′, i.e., WD1′ is more sensitive to variations of Γ_c. The opposite behavior has been observed in steady-state, but this is probably due to the modifications for normalization with respect to speed.

3) Load Imbalance: The two fault indicators WD1′ and WD2′ are tested with a load imbalance of theoretical amplitude 0.1 N · m. In this configuration, the DC motor is directly connected to the resistor without the DC/DC converter, i.e., the load torque is no longer constant but proportional to speed during the transients. The chosen speed profile is identical to the preceding cases. At full speed, the load is 10% of the nominal load in these tests.

The obtained results with the two fault indicators are displayed in Fig. 17 for the healthy drive and with a load imbalance. It can be noticed with the two indicators that the healthy and faulty cases can be distinguished at low speed and full speed. However, at certain supply frequencies around 35 Hz, this is not clearly possible. This phenomena has also been studied in steady state and the same results observed: For supply frequencies around 35 Hz, all indicators show no significant variation between the healthy and the faulty cases. The exact reasons are unknown to the authors, but possible causes could be resonances or antiresonances of the test rig mechanical structure that are excited at these frequencies.

Nevertheless, the mean indicator value increased during one speed cycle by 28% with WD1′ and by 52% with WD2′. This demonstrates that realistic mechanical faults can be detected during transients using time–frequency methods.

VI. Conclusion

This paper studies the detection of mechanical faults in induction motor drives at variable speed using stator current time–frequency analysis with the WD. The fault-related torque oscillations modulate the phase of the stator current signal and lead to a characteristic signature on the WD. Fault indicators can be calculated using properties of this interference structure. The two proposed methods and a classical spectrum-based indicator are implemented on a DSP for on-line condition monitoring. Experimental investigations in steady-state show that load imbalance and small torque oscillations can be detected. During speed transients, the distinction between the healthy and faulty cases is more difficult but still possible. Therefore, the practical feasibility of using time–frequency methods for on-line motor condition monitoring during transients has been demonstrated.

References

[1] W. T. Thomson, "On-line current monitoring to detect electrical and mechanical faults in three-phase induction motor drives," in *Proc. Int. Conf. Life Manage. Power Plants*, Dec. 1994, pp. 66–73.

[2] S. F. Legowski, A. H. M. S. Ula, and A. M. Trzynadlowski, "Instantaneous power as a medium for the signature analysis of induction motors," *IEEE Trans. Ind. Appl.*, vol. 32, no. 4, pp. 904–909, Jul./Aug. 1996.

[3] C. Kral, T. G. Habetler, and R. G. Harley, "Detection of mechanical imbalances of induction machines without spectral analysis of time-domain signals," *IEEE Trans. Ind. Appl.*, vol. 40, no. 4, pp. 1101–1106, Jul./Aug. 2004.

[4] R. R. Obaid, T. G. Habetler, and D. J. Gritter, "A simplified technique for detecting mechanical faults using stator current in small induction motors," in *Conf. Rec. IAS Annu. Meeting*, Rome, Italy, Oct. 2000, pp. 479–483.

[5] S. Rajagopalan, J. A. Restrepo, J. M. Aller, T. G. Habetler, and R. G. Harley, "Wigner-Ville distributions for detection of rotor faults in brushless DC (BLDC) motors operating under non-stationary conditions," in *Proc. IEEE Int. SDEMPED*, Vienna, Austria, Sep. 2005, pp. 313–319.
[6] M. Blödt, M. Chabert, J. Faucher, and B. Dagues, "Mechanical load fault detection in induction motors by stator current time-frequency analysis," in *Proc. IEEE IEMDC*, San Antonio, TX, May 2005, pp. 1881–1888.
[7] M. Blödt, M. Chabert, J. Regnier, J. Faucher, and B. Dagues, "Detection of mechanical load faults in induction motors at variable speed using stator current time-frequency analysis," in *Proc. IEEE Int. SDEMPED*, Vienna, Austria, Sep. 2005, pp. 229–234.
[8] J. R. Cameron and W. T. Thomson, "Vibration and current monitoring for detecting airgap eccentricity in large induction motors," *Proc. Inst. Electr. Eng.*, vol. 133, no. 3, pp. 155–163, May 1986.
[9] B. Heller and V. Hamata, *Harmonic Field Effects in Induction Machines*. Amsterdam, The Netherlands: Elsevier, 1977.
[10] M. Blödt, P. Granjon, B. Raison, and G. Rostaing, "Models for bearing damage detection in induction motors using stator current monitoring," in *Proc. IEEE ISIE*, Ajaccio, France, May 2004, pp. 383–388.
[11] B. Boashash, *Time Frequency Signal Analysis and Processing—A Comprehensive Reference*, 1st ed. Oxford, U.K.: Elsevier, 2003.
[12] P. Flandrin, *Time-Frequency/Time-Scale Analysis*. San Diego, CA: Academic, 1999.
[13] K. Bacha, M. Gossa, H. Henao, and G. A. Capolino, "A time-frequency method for multiple fault detection in three-phase induction machines," in *Proc. IEEE Int. SDEMPED*, Vienna, Austria, Sep. 2005, pp. 361–366.
[14] E. Wigner, "On the quantum correction for thermodynamic equilibrium," *Phys. Rev.*, vol. 40, no. 5, pp. 749–759, Jun. 1932.
[15] J. Ville, "Théorie et applications de la notion de signal analytique," *Câbles Transm.*, vol. 2, no. 1, pp. 61–74, 1948.
[16] W. Mecklenbräuker and F. Hlawatsch, Eds., *The Wigner Distribution—Theory and Applications in Signal Processing*. Amsterdam, The Netherlands: Elsevier 1997.
[17] D. L. Jones and T. W. Parks, "A resolution comparison of several time-frequency representations," *IEEE Trans. Signal Process.*, vol. 40, no. 2, pp. 413–420, Feb. 1992.
[18] M. Abramowitz and I. A. Stegun, *Handbook of Mathematical Functions With Formulas, Graphs, and Mathematical Tables*, 9th ed. New York: Dover, 1964.
[19] F. Auger, P. Flandrin, P. Gonçalvès, and O. Lemoine, *Time-Frequency Toolbox*. France: CNRS/Rice Univ., 1995/1996. [Online]. Available: http://tftb.nongnu.org
[20] M. Blödt, J. Regnier, M. Chabert, and J. Faucher, "Fault indicators for stator current based detection of torque oscillations in induction motors at variable speed using time-frequency analysis," in *Proc. IEE 3rd Int. Conf. PEMD*, Dublin, Ireland, Apr. 2006, pp. 56–60.

Martin Blödt (S'04) was born in Baden-Baden, Germany, in 1978. He received the double diploma degree in electrical engineering from the University of Karlsruhe, Karlsruhe, Germany, and from the Institut National Polytechnique de Grenoble, Grenoble, France, both in 2003 and the Ph.D. degree from the Institut National Polytechnique de Toulouse, Toulouse, France, in 2006.

From 2003 to 2006, he was with the Laboratoire d'Electrotechnique et d'Electronique Industrielle (LEEI), Institut National Polytechnique de Toulouse. Since 2007, he has been with Siemens AG. His research interests are fault diagnosis in electrical machines and suitable signal processing methods such as time-frequency signal processing and parameter estimation.

David Bonacci was born in 1974. He received the Engineering degree from the Ecole Nationale Supérieure d'Electrotechnique, d'Electronique, d'Informatique, d'Hydraulique et des Télécommunications (ENSEEIHT), Toulouse, France, in 1999, and the Ph.D. degree from the Institut National Polytechnique of Toulouse, Toulouse, in 2003.

He was a Research Associate at the engineering school ENSEEIHT in 2004 and 2005. He is currently a Research Engineer at the Télécommunications Spatiales et Aéronautiques (TéSA) Laboratory, Toulouse. He is still teaching signal processing and telecommunications at the undergraduate and graduate level. His research activity is centered around radar, spectral analysis, parametric modeling, subband decomposition, and condition monitoring.

Jérémi Regnier received the Ph.D. degree in electrical engineering from the Institut National Polytechnique of Toulouse, Toulouse, France, in 2003.

Since 2004, he is working as Assistant Professor at the Electrical Engineering and Control Systems Department. He is also a Researcher at the Laboratoire d'Electrotechnique et d'Electronique Industrielle, Toulouse. His research interests are modeling and simulation of faulty electrical machines and drives as well as the development of monitoring techniques using signal processing methods.

Marie Chabert was born in 1970. She received the Engineering degree from the engineering school Ecole Nationale Supérieure d'Electrotechnique, d'Electronique, d'Informatique, d'Hydraulique et des Télécommunications (ENSEEIHT), Toulouse, France, in 1994 and the Ph.D. degree from Institut National Polytechnique de Toulouse, Toulouse, in 1997.

She joined ENSEEIHT in 1998 as an Assistant Professor. She teaches signal and image processing and telecommunications at the undergraduate and graduate level. Her research activity is centered around estimation, detection and wavelet transform. She coauthored about 30 communications and papers in signal processing conferences and journals.

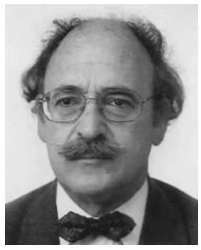

Jean Faucher (M'06) received the diploma degree in electrical engineering from Institut National Polytechnique de Toulouse (INP Toulouse), Toulouse, France, in 1967, and the Docteur-Ingénieur (Ph.D.) and Docteur ès Sciences on switched reluctance machines in 1969 and 1981, respectively.

Since 1985, he is a Full University Professor at INP Toulouse, teaching electrical and control engineering. He is a Researcher at the laboratory LEEI in Toulouse. His main fields of interest concern information processing and modeling of electrical machines and static converters for fault diagnosis, monitoring and simulation. He is in charge of international relationships for INP Toulouse.